

ABSTRACT

CHATTERJEE, PUNNAG. Structural Modeling of a Compliant Flexure Flow Energy Harvester. (Under the supervision of Dr. Matthew Bryant).

This thesis presents the concept of a flow-induced vibration energy harvester based on a one-piece compliant flexure structure. This energy harvester utilizes the aeroelastic flutter phenomenon to convert flow energy to structural vibrational energy and to electrical power output through piezoelectric transducers. This flexure creates a discontinuity in the structural stiffness and geometry that can be used to tailor the mode shapes and natural frequencies of the device to the desired operating flow regime while eliminating the need for discrete hinges that are subject to fouling and friction. An approximate representation of the flexure rigidity is developed from the flexure link geometry, and a model of the complete discontinuous structure and integrated flexure is formulated based on transfer matrix method. The natural frequencies and mode shapes predicted by the model are validated using finite element simulations and are shown to be in close agreement. A proof-of-concept energy harvester incorporating the proposed flexure design has been fabricated and investigated in wind tunnel testing. The aeroelastic modal convergence, critical flutter wind speed, power output and limit cycle behavior of this device is experimentally determined and discussed.

© Copyright 2015 Punnag Chatterjee
All Rights Reserved

Structural Modeling of a Compliant Flexure Flow Energy Harvester

by
Punnag Chatterjee

A thesis submitted to the Graduate Faculty of
North Carolina State University
in partial fulfillment of the
requirements for the Degree of
Master of Science

Mechanical Engineering

Raleigh, North Carolina

2015

APPROVED BY:

Dr. Richard Keltie

Dr. Ashok Gopalarathnam

Dr. Matthew Bryant
Chair of Advisory Committee

BIOGRAPHY

Punnag Chatterjee was born in Kolkata, West Bengal, India. He attended National Institute of Technology - Durgapur, where he earned his Bachelor of Technology in Mechanical Engineering in 2010. He then joined the R&D division of a leading automobile industry in India, Bajaj Auto Limited as a vehicle suspension design engineer. He worked for three years designing suspension springs, compliant bushes, iterating on suspension hardpoints, coordinating with durability and performance testing of suspension components with the testing team, finalizing design and coordinating with vendor for part development and manufacture. He started his MS degree at ISSRL at NC State University in August 2013. In a broader sense his research focus was primarily on energy harvesting from ambient flow vibrations and base excitations. Apart from research he is interested in camping, hiking, biking and travelling.

ACKNOWLEDGMENTS

I would firstly like to thank my mother, Kalyani Chatterjee. She not only supported my education but also provided me with moral support through all stages of my life. Her contribution in my life cannot be explained in words. I would also like to thank my wife Abhisha, for not allowing me to do anything except for concentrating on my thesis presentation during the days leading up to my defense.

I would like to thank Dr. Bryant for providing a well-equipped lab, excellent mentorship and guidance as my advisor and constructive feedback which helped me improve my skills as a researcher. I would like to specifically thank him for encouraging me to explore new research ideas.

Thanks to Dr. Keltie and Dr. Gopalarathnam for serving on my advisory committee.

A special thanks to my current labmates Edward Chapman, Benjamin Kirschmeier, Marc Macleod and Tyler Jenkins for helping me with constructive feedback on my research presentations and also for all of the laughs we shared. Working in ISRRL would not have been the same experience without you guys.

I gratefully acknowledge funding support for this research from the National Science Foundation under Award No. CMMI-1435077 and Program Officer Massimo Ruzzene. Additional funding was provided by the North Carolina Space Grant 2014 New Investigator Award.

TABLE OF CONTENTS

LIST OF TABLES	iv
LIST OF FIGURES	v
1. Introduction	1
2. System Model and Problem Formulation	4
2.1. <i>Device Concept and Configuration</i>	4
2.2. <i>Flexure Segment Configuration and Model</i>	6
2.3. <i>Structural Model of the Device using Transfer matrix Method</i>	11
2.4. <i>Electromechanical Model of the Structure</i>	20
3. Model Validation and Verification	22
4. Experimental setup and results	26
4.1. <i>Modal Convergence Investigation</i>	28
4.2. <i>LCO Investigation</i>	30
5. Conclusion	32
REFERENCES	34

LIST OF TABLES

Table 1. Geometrical dimensions and mechanical properties of the structure.....	21
Table 2. Electromechanical properties and geometric dimensions of Mide QP 16N.	22
Table 3. Verification of analytically obtained short circuit natural frequencies of the system.	23
Table 4. Comparison of experimental and analytical natural frequencies.	27

LIST OF FIGURES

Figure 1. Geometry and schematic of the energy harvesting device showing the different segments and corresponding dimensions. (1) Piezo-beam segment (2) beam segment (3) flexure segment, (4) flap connector segment, and (5) flap segment.	4
Figure 2. Fabricated flexure segment showing the individual torsion links of length ls connected to inner and outer junctions.	6
Figure 3. Schematic representation of the flexure segment model. The flexure is discretized as a system of rigid links, each of length lr , connected by torsional springs of stiffness $k\theta$, represented here as black dots.....	8
Figure 4. Comparison of flexure model with FE model simulated in ANSYS. Tip deflection of cantilevered flexure section is plotted as a function of number of rigid links.....	11
Figure 5. Enlarged view of segment 5 is provided, showing the local beam coordinate system.	13
Figure 6. Side view schematic of the structure with the bimorph piezoelectric patches laminated to the top and bottom surfaces of the substrate.	13
Figure 7. Comparison of Mode Shapes obtained through TMM with FE simulation. Colors in the analytical model correspond to the different segments of the structure used in TMM modeling.	23
Figure 8. Effect of the geometric parameter like the torsional link length on the modal natural frequencies of the system.....	24
Figure 9. Effect of the geometric parameter like the number of rigid links on the modal natural frequencies of the system.....	25
Figure 10. Physical structure as mounted in the wind tunnel test section. Beam deflection response is measured at the point specified in Figure 1	26
Figure 11. Effect of varying wind speeds on first two natural frequencies of the structure, showing (A) externally excited and (B) self-excited flutter locations. This plot also shows the estimated error in measurements via error bars representing one SD in each direction vertically.	29
Figure 12. This figure plots the average power output of the structure as a function of resistive load for three different wind speeds, U	30
Figure 13. This figure plots the beam tip response and average power output of the structure as a function of wind speed. The beam tip deflection is measured at the point specified in Figure 10	31

1. Introduction

Designing a piezoelectric vibration energy harvester has been a subject of considerable interest over the past two decades [1]. While various sources of vibration excitation can provide the input to such energy harvesters, flow-induced aeroelastic oscillation phenomena have attracted substantial research work in recent years. Researchers have proposed fluttering energy harvesters based on mechanisms like a bio inspired leaf [2], airfoil section [3] or rigid flap [4,5] attached at the end of a cantilever piezoelectric bender. These designs behave as discrete two degree of freedom (DOF) systems with one DOF originating from the cantilever (typically in the first vibration mode) and a second, coupled DOF from the ball bearings or hinges that create a rotational DOF between the cantilever and the attached airfoil or flap. This arrangement creates an aeroelastic system with a heaving and a pitching DOF that, when properly designed, can harvest energy over a range of flow speeds due to stable flow-excited limit cycle oscillation (LCO).

Researchers have also extracted power from aeroelastic LCO of structures like cantilevered thin plates [6,7] or a compliant heavy flag hosting an IPMC [8]. These devices exhibit flag-like oscillations in a continuous, distributed parameter structure. Researchers have also cleverly designed a piezoelectric cantilevered beam to resemble a T-shape at the free end to extract power from ambient fluid flow [9]. In comparison to the discrete two DOF harvesters, flag-like devices offer simplicity and eliminate the need for assembling multiple discrete parts. In addition, the use of pin hinges or bearings in the discrete two DOF designs could pose problems in dirty or dusty environments, underwater, or in extreme temperatures where the conditions are detrimental to the functionality of rotational joints. However, the simplistic

morphology of a flag-like harvester also presents a limited choice of design parameters available to optimize the device to a given flow environment. The two DOF designs on the other hand, can use a variety of parameters including the pitch/heave natural frequency ratio, inertial coupling parameters and flap geometry to minimize cut-in wind speed while maintaining compact size and high natural frequency, which is advantageous for efficiency [10]. In addition, a recent comparison of literature on experimental results [11] showed that a two DOF aeroelastic harvester achieved higher conversion efficiency than other aeroelastic harvesters of similar size.

In this thesis, we develop a modeling methodology for a piezostucture incorporating stepped cross-sections and a compliant flexure mechanism into a one-piece substrate. This allows tailoring of the device mode shapes, natural frequencies, and aeroelastic modal convergence behavior in a ‘solid-state’ aeroelastic energy harvester that combines the attributes of flag-like and two DOF designs. Compliant flexure hinges have several advantages over conventional joints. They are frictionless and precise in operation, lightweight and compact. Moreover, they are exempt from the need to provide for lubrication and sealing. Hence, flexure hinges are a promising proposition and such hinges have found numerous nano-manufacturing [12] and piezo actuator applications [13] especially in MEMS [14]. It has also been shown that the performance and operational life of such hinges could be modeled analytically to closely agree with the experimental results and when designed properly, also have an excellent fatigue life [15].

Discrete, two DOF pitch-heave aeroelastic systems such as the so-called typical section of a wing are traditionally modeled using energy methods [16]. Likewise, similar methods, in

combination with Rayleigh-Ritz piezoelectric beam models, have been accurately applied to two DOF aeroelastic energy harvester designs [4]. This formulation represents the beam tip deflection as the aeroelastic heave coordinate and the flap hinge angle as the pitch coordinate. However, when the discrete revolute joint is replaced by an integrated flexure having multiple geometric discontinuities, it is not prudent or valid to functionally decouple the system into distinct beam and flap segment. The flexure joining the beam segment with the flap segment cannot be assumed to be a pure revolute joint, but rather acts as a distributed component with its own dynamic properties that affect the mode shapes and natural frequencies of the complete structure. It is also to be noted that the location of the flap rotation axis is no longer geometrically fixed as in an aeroelastic typical section, but rather depends on the deformation of the flexure. These modeling challenges motivate a methodology to analytically predict the mode shapes and natural frequencies of the complete structure. In addition to this analytical treatment, the aeroelastic behavior and energy harvesting capability of a proof-of-concept device is investigated experimentally to establish the feasibility of such a design.

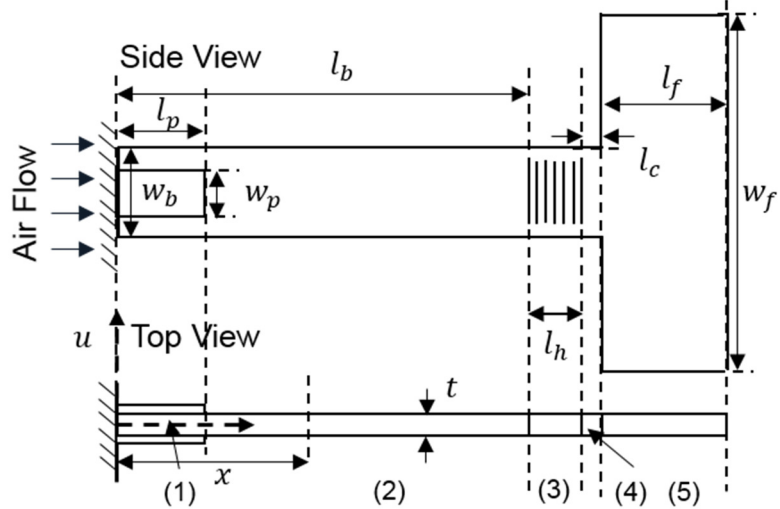


Figure 1. Geometry and schematic of the energy harvesting device showing the different segments and corresponding dimensions. (1) Piezo-beam segment (2) beam segment (3) flexure segment, (4) flap connector segment, and (5) flap segment.

2. System Model and Problem Formulation

2.1. Device Concept and Configuration

In order to produce flutter oscillations, the energy harvesting structure must be designed to create two closely spaced natural frequencies that coalesce under the influence of increasing flow speeds and aerodynamic forces. In traditional aeroelastic modeling of aircraft wings and tails, these frequencies correspond to the pitching and heaving degrees of freedom of an airfoil section supported by linear and torsional springs [16]. A chordwise mass-imbalance couples the degrees of freedom and the separation between airfoil aerodynamic center and the pitch center of rotation causes pitch stiffness to change with ambient flow speed. While aircraft designers clearly seek to avoid aeroelastic oscillation, when properly implemented in an energy

harvester, self-excited oscillations are initiated above a critical wind speed and stable LCO due to structural and aerodynamic nonlinearities occur over a wide range of speeds.

The energy harvesting structure is shown schematically in Figure 1, at zero-flow condition where the device is stationary. In order to make this device operational, it is placed axially in the direction of flow, such that the clamped root of structure is oriented upstream and the free end downstream. The energy harvester is assumed to be composed of a one-piece elastic substrate sheet that has been cut or stamped into a planform with stepped widths as shown. Piezoelectric patches of arbitrary thickness and coverage length are assumed to be laminated at the root of the structure in a bimorph fashion to provide electromechanical transduction. To create an abrupt change in the out-of-plane bending rigidity of the structure, a series of patterned cuts are integrated into the substrate, creating a compliant flexure segment and dividing the structure into a ‘beam segment’ upstream and a ‘flap segment’ downstream. Compared to previous modal convergence flutter energy harvesters, which used a discrete pin or ball-bearing hinge assembly between a beam and wing [2–4,17] this design offers simplicity and reduced friction. Rolling or sliding surfaces prone to fouling are eliminated and the total number of parts in the harvester is reduced by an order of magnitude compared to ball-bearing designs [4].

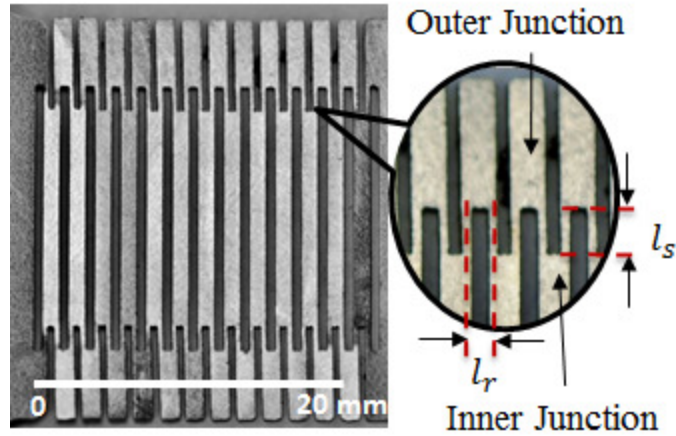


Figure 2. Fabricated flexure segment showing the individual torsion links of length l_s connected to inner and outer junctions.

2.2. Flexure Segment Configuration and Model

The flexure segment causes an abrupt change in the bending rigidity of the structure that will in turn be reflected in the mode shapes and natural frequencies of the complete structure. At the same time, this segment should maintain sufficient stiffness against deformation in other directions such as in-plane bending and out-of-plane torsion to prevent undesired vibrations. For a given substrate sheet material, the overall stiffness of the flexure segment in bending will be determined by the size, number, and shape of the patterned cuts made in the sheet. Here, we consider a patterned flexure geometry composed of repeating torsion bar links and connecting junctions, implemented as a joined upper and lower zigzag configuration. **Figure 2** shows a photograph of such a flexure pattern that has been laser-cut from a sheet of hard tempered stainless steel. When the flap segment is transversely displaced from its mean position, the flexure segment undergoes transverse bending. It is assumed that the torsion links have the least sectional modulus, and are the most compliant portions of this segment. Therefore, we

assume that only these links twist and deform while the inner and outer junctions remain rigid. Thus the junctions behave like rigid links connected by torsional springs at either end. The overall deflection of the flexure segment is facilitated by each of these torsional springs which are connected in parallel across the width direction and in series along the longitudinal direction.

To further facilitate implementation into the full structural model to be developed in Section 2.3, we propose that the bending of the flexure segment can be approximated by an effective beam element. Hence, the entire segment is represented by a beam with a constant cross section along its length, and having an effective bending rigidity and effective mass per unit length derived from the geometry of the actual flexure pattern. The advantage of performing this approximation is twofold, firstly it eliminates cumbersome modelling of each torsion bar and connecting element in the distributed parameter structure and secondly it saves computational cost in the complete model so that design parameter variations can be quickly considered. This assumption is validated against a finite element (FE) analysis of the full flexure geometry in static bending at the end of this segment, and also in the mode shape analysis of the complete structure presented in Section 3.

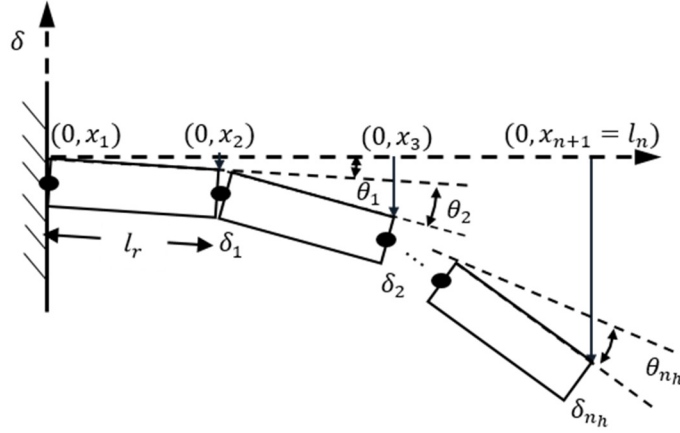


Figure 3. Schematic representation of the flexure segment model. The flexure is discretized as a system of rigid links, each of length l_r , connected by torsional springs of stiffness k_θ , represented here as black dots.

In order to derive the effective bending rigidity, the patterned flexure segment of length l_h is discretized into n_h rigid links each having an elemental length of l_r . Each of these elemental links is connected to the preceding link with a rotational spring of stiffness k_θ . **Figure 3** shows this arrangement of links and rotational springs cantilevered from a wall and bending due to a load P applied at the tip of rigid element n_h . Under these conditions, the tip deflection of the discretized structure undergoing bending is given by

$$\delta_{n_h} = \sum_{j=1}^{n_h} l_r \sin \left(\sum_{p=1}^j \theta_p \right) \quad (1)$$

Balancing the moment acting across the tip and root of the i^{th} rigid element gives us the torsional rotation of the i^{th} spring as

$$\theta_i = \frac{P(l_h - x_i)}{k_\theta} \quad (2)$$

Assuming small angles and neglecting the effect of geometric foreshortening under large deflections, the effective linear tip stiffness of the discretized structure is given by K_l . This can be further equated to the linear tip stiffness of an equivalent beam of length l_h and with the same cantilevered boundary conditions.

$$K_l = \frac{P}{\delta_{n_h}} = \frac{6k_\theta}{l_r [3l_h n_h (n_h + 1) - l_r (n_h - 1)n_h (n_h + 1)]} \quad (3)$$

$$= \frac{3(EI)_e}{l_h^3}$$

Thus, the effective bending rigidity of the flexure segment, $(EI)_e$, can now be written as

$$(EI)_e = \frac{2k_\theta l_h^3}{l_r n_h (n_h + 1) [3l_h - l_r (n_h - 1)]} \quad (4)$$

This equation is useful as it relates the geometric properties of the flexure hinge to that of the bending rigidity of this segment, facilitating the tuning of the flexure segment to affect the desired natural frequencies of the entire structure. In other words tuning the flexure hinge would allow the system to be optimized for efficient power extraction for a specific environment with its own flow regime. The methodology discussed above is not restricted or specific to the design under consideration but can be extended to other flexure designs composed of repeating torsion links and rigid segments. As we can see from equation (4), the only inputs are the length of the repetitive rigid link l_r and the torsional stiffness of the connectors, k_θ . Therefore, the immediate limitation of using this equation is the accuracy with which the torsional link stiffness, k_θ can be determined. The value of k_θ for the prismatic torsion links used in this structure can be calculated as

$$k_{\theta} = \frac{2GJ}{l_e} \quad (5)$$

where J represents the torsion factor of the torsional link, having a square cross section of 0.38 mm which is also equal to the thickness of the substrate under consideration here. Neglecting the effect of restrained warping at the end of the torsional link, the torsion factor can be easily calculated [18] from De Saint Venant's torsion theory for free warping

$$J = \frac{t^4}{3} - 0.1928t^4 \quad (6)$$

In order to validate the applicability of the flexure model discussed above, it is compared and verified with a FE model implemented in ANSYS (Workbench version 14.5). The flexure segment is isolated and treated separately in this analysis. The FE analysis is performed with the actual 3D model of the flexure where the root end is clamped and a known load is applied at the tip of this flexure. The analysis restricts the tip deflection within the elastic limit of the material and also within the experimentally observed envelope of the flexure tip deflection during LCO. **Figure 4** shows the accuracy of the flexure segment model when the number of repeated torsional links are varied from 4, representing a flexure segment which is almost as rigid as a beam, to 32, representing a very flexible segment which responds very easily towards a bending load. The FE results are compared with the analytical results for three different tip loads of 0.1 N, 0.3 N and 0.5 N, and in all these cases the analytical results show very close agreement with the FE results for fairly large tip deflections up to 10mm. It can be seen that the analytical model is able to predict the nonlinearly increasing tip deflection with a linear increment of the number of torsion links, keeping all other geometric dimensions of the flexure constant.

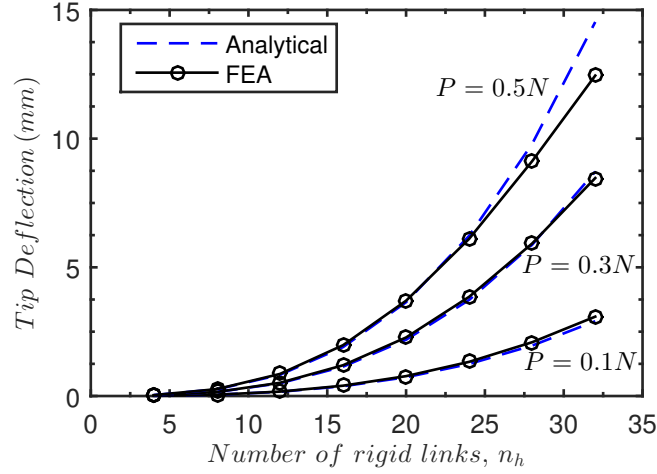


Figure 4. Comparison of flexure model with FE model simulated in ANSYS. Tip deflection of cantilevered flexure section is plotted as a function of number of rigid links.

2.3. Structural Model of the Device using Transfer matrix Method

The model of the complete structure must account for multiple discontinuities in the structure resulting from partial piezo-patch coverage and abrupt changes in the geometric cross section. For this purpose a well-established, Transfer Matrix Method (TMM) has been incorporated to analytically model the device and extract the mode shape of the entire structure. Originally conceived by Pestel and Leckie [19], TMM has been used successfully in a wide range of applications including modeling tapered beam-like structures [20], modeling complicated zig-zag structures [21], and detecting cracks in beams from vibration responses [22]. TMM presents an advantage over conventional FE methods in the sense that the increased complexity of the structure does not increase the size of the eigenvalue problem, saving

computational cost. In this thesis the TMM piezoelectric model developed by Wickenheiser [23], has been applied to model the energy harvester and predict the mode shapes and the natural frequencies of the structure. This method is based on Euler-Bernoulli beam theory and provides the capability to model arbitrary angles between different beam segments, lumped mass, thickness and material discontinuities in the structure.

Let $u(x, t)$ be the transverse displacement of the structure, from side view of **Figure 1**, this displacement would be into or out of the plane of the paper. Using the method of variable separation this deflection is decomposed into its constituent components of time and space.

$$u(x, t) = \sum_{r=1}^{\infty} \eta_r(t) \phi_r(x) = \underline{\eta}(t) \underline{\phi}(x) \quad (7)$$

where, $\eta_r(t)$ and $\phi_r(x)$ are the r^{th} modal amplitude and mode shape function respectively.

For this method to be applicable, the full structure is discretized into smaller beam segments which exhibit uniformity of both geometric and material properties, such that each has a constant cross section and uniform bending stiffness and mass per unit length along the length of this segment. Conceptually, this method relates the two state vectors corresponding to two subsequent points on the structure through a state transition matrix. It provides a systematic approach to computing the state transfer matrix, also called a global transfer matrix, which is applicable to the entire structure as one moves from one end to the other along the longitudinal direction. The state vector is compiled from the six independent variables arising from the six coupled equations of Euler-Bernoulli beam theory. These six states are $\psi, N, \phi_r, d\phi_r/dx, M$ and V , defined as the axial displacement shape function, normal axial

force, transverse displacement shape function, slope of transverse displacement, internal bending moment and internal shear force respectively.

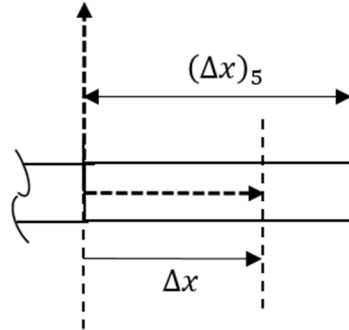


Figure 5. Enlarged view of segment 5 is provided, showing the local beam coordinate system.

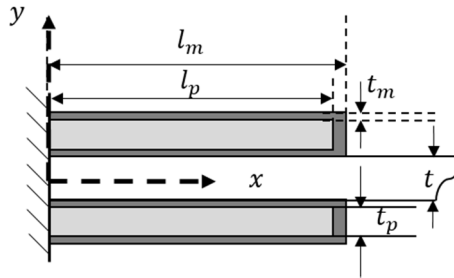


Figure 6. Side view schematic of the structure with the bimorph piezoelectric patches laminated to the top and bottom surfaces of the substrate.

The field transfer matrix for each piece-wise continuous segment is given by

$$[F_j(\Delta x, \omega_r)] = \begin{bmatrix} 1 & 0 & 0 & 0 & 0 & 0 \\ (\Delta x)(\rho A)_j \omega_r^2 & 1 & 0 & 0 & 0 & 0 \\ 0 & 0 & c_0 & (\Delta x)c_1 & \frac{(\Delta x)^2}{(EI)_j} c_3 & -\frac{(\Delta x)^3}{(EI)_j} c_3 \\ 0 & 0 & \frac{(\Delta x)^3 (\rho A)_j \omega_r^2}{(EI)_j} c_3 & c_0 & \frac{(\Delta x)}{(EI)_j} c_1 & -\frac{(\Delta x)^2}{(EI)_j} c_2 \\ 0 & 0 & (\Delta x)^2 (\rho A)_j \omega_r^2 c_2 & (\Delta x)^3 (\rho A)_j \omega_r^2 c_3 & c_0 & -(\Delta x)c_1 \\ 0 & 0 & -(\Delta x)(\rho A)_j \omega_r^2 c_1 & -(\Delta x)^2 (\rho A)_j \omega_r^2 c_2 & -\frac{(\Delta x)^3 (\rho A)_j \omega_r^2}{(EI)_j} c_3 & c_0 \end{bmatrix} \quad (8)$$

The Field Transfer Matrix F_j is a function of the system natural frequency ω_r associated with the r^{th} mode shape function, ϕ_r , and Δx . The subscript j represents the j^{th} beam segment starting from the root of the structure and Δx is the local, longitudinal coordinate distance of j^{th} beam segment, as shown in Figure 5.

where,

$$\begin{aligned} c_0 &= \frac{1}{2} [\cosh\{\beta_j \Delta x\} + \cos\{\beta_j \Delta x\}] \\ c_1 &= \frac{1}{2(\beta \Delta x)} \{\sinh\{\beta_j \Delta x\} + \sin\{\beta_j \Delta x\}\} \\ c_2 &= \frac{1}{2(\beta \Delta x)^2} \{\cosh\{\beta_j \Delta x\} - \cos\{\beta_j \Delta x\}\} \\ c_3 &= \frac{1}{2(\beta \Delta x)^3} \{\sinh\{\beta_j \Delta x\} - \sin\{\beta_j \Delta x\}\} \end{aligned} \quad (9)$$

the term β_j appearing in equation (9) is related to the system natural frequency by the ratio of segmental mass per unit length, $(\rho A)_j$ over segmental bending stiffness, $(EI)_j$ as shown below

$$\beta_j^4 = \frac{(\rho A)_j}{(EI)_j} \omega_r^2 \quad (10)$$

In addition to the FTM's, Point Transfer Matrices (PTM's) can also be incorporated in order to model the discontinuities between adjacent beam segments arising out of lumped masses or bends in the structure which results in a jump in internal forces and moments [23]. The PTMs are calculated by

$$[P_j(\omega_r)] = \begin{bmatrix} \cos\theta_j & 0 & \sin\theta_j & 0 & 0 & 0 \\ m_j\omega_r^2\cos\theta_j & \cos\theta_j & m_j\omega_r^2\sin\theta_j & 0 & 0 & \sin\theta_j \\ -\sin\theta_j & 0 & \cos\theta_j & 0 & 0 & 0 \\ 0 & 0 & 0 & 1 & 0 & 0 \\ 0 & 0 & 0 & -I_j\omega_r^2 & 1 & 0 \\ -m_j\omega_r^2\sin\theta_j & -\sin\theta_j & m_j\omega_r^2\cos\theta_j & 0 & 0 & \cos\theta_j \end{bmatrix} \quad (11)$$

where m_j is the lumped mass at the end of j^{th} segment, I_j is the lumped moment of inertia at the joint and θ_j is the relative angle between beam segments j and $j + 1$, measured at initial equilibrium position. For the structure under consideration here, $m_j = \theta_j = 0$, for which the PTM's reduce to the identity matrix.

Once all the FTM's and PTM's of the structure are calculated, these matrices can be assembled together to form the global transfer matrix as

$$[U(\omega_r)] = \prod_{j=n}^1 [P_j(\omega_r)] [F_j((\Delta x)_j, \omega_r)] \quad (12)$$

where $(\Delta x)_j$ is the total segmental length of j^{th} segment. This ensures that the 6x6 global transfer matrix, U is only a function of the r th system natural frequency, ω_r , which is still unknown.

With the global transfer matrix calculated, it is now possible to relate the six independent state variables at the root of the structure with those at the tip of the structure.

$$\begin{Bmatrix} \psi(L_n) \\ N(L_n) \\ \phi_r(L_n) \\ d\phi_r(L_n)/dx \\ M(L_n) \\ V(L_n) \end{Bmatrix} = [U(\omega_r)] \begin{Bmatrix} \psi(0) \\ N(0) \\ \phi_r(0) \\ d\phi_r(0)/dx \\ M(0) \\ V(0) \end{Bmatrix} \quad (13)$$

It is now necessary to impose the boundary conditions at either end of the entire structure to provide information about some of the state variables. The structure in consideration has end conditions akin to a cantilevered beam, where the root of the structure is fixed at the clamp ($x = 0$) and the tip of the structure ($x = L_n = l_b + l_h + l_c + l_f$) is free. At the root, the boundary conditions dictate that

$$\phi(0) = \phi(0) = \frac{d\phi(0)}{dx} = 0 \quad (14)$$

At the tip or the free end, the known states are

$$N(L_n) = M(L_n) = V(L_n) = 0 \quad (15)$$

Applying the boundary conditions in equation (13) and considering only the second, fifth and sixth linear equations, we get the resulting characteristic equation of the system

$$\begin{Bmatrix} 0 \\ 0 \\ 0 \end{Bmatrix} = \begin{bmatrix} U_{2,2} & U_{2,5} & U_{2,6} \\ U_{5,2} & U_{5,5} & U_{5,6} \\ U_{6,2} & U_{6,5} & U_{6,6} \end{bmatrix} \begin{Bmatrix} N(0) \\ M(0) \\ V(0) \end{Bmatrix} \quad (16)$$

where $U_{r,c}$ represents the element at r^{th} row and c^{th} column of the global transfer matrix, $[U(\omega_r)]$.

Taking the determinant of the 3x3 matrix in equation (16) yields a polynomial equation in ω_r , solving for which gives the roots of the equations which are actually the short circuit natural frequencies of the system.

Now that the modal natural frequencies are known, the transverse mode shapes corresponding to the r^{th} natural frequency ω_r can be evaluated

$$\begin{Bmatrix} \psi(L_n) \\ N(L_n) \\ \phi_r(L_n) \\ d\phi_r(L_n)/dx \\ M(L_n) \\ V(L_n) \end{Bmatrix} = [\mu(x)] \begin{Bmatrix} \psi(0) \\ N(0) \\ \phi_r(0) \\ d\phi_r(0)/dx \\ M(0) \\ V(0) \end{Bmatrix} \quad (17)$$

If the complete structure is composed of n segments and the global longitudinal coordinate, x , lies within beam segment γ ($1 \leq \gamma \leq n$), then

$$[\mu(x)] = [P_\gamma(\omega_r)][F_\gamma(\Delta x, \omega_r)][T] \quad (18)$$

where,

$$\Delta x = \begin{cases} \Delta x & \text{for } \gamma = 1 \\ x - \sum_{j=1}^{\gamma-1} (\Delta x)_j & \text{for } 1 < \gamma \leq n \end{cases} \quad (19)$$

and T is a 6x6 matrix composed of known values, calculated as

$$[T] = \begin{cases} I & \text{for } \gamma = 1 \\ \prod_{j=\gamma-1}^1 [P_j(\omega_r)][F_j((\Delta x)_j, \omega_r)] & \text{for } 1 < \gamma \leq n \end{cases} \quad (20)$$

where I is a 6x6 identity matrix.

Employing the third linear equation within equation (17) and performing mathematical manipulations we obtain

$$\phi_{r\gamma}(\Delta x) = \left\{ -(k_1 + \sigma k_2) [\mu(x)]_{3,2} + [\mu(x)]_{3,5} + \sigma [\mu(x)]_{3,5} \right\} M(0) \quad (21)$$

and the overall mode shape function of the structure is given by

$$\phi_r(x) = \{ \phi_{r1}(\Delta x), \phi_{r2}(\Delta x), \phi_{r3}(\Delta x), \dots, \phi_{rm}(\Delta x) \} \quad (22)$$

where $[\mu(x)]_{r,c}$ represents the element at r^{th} row and c^{th} column of the 6x6 matrix, $[\mu(x)]$.

The above mentioned methodology is used to compute the transverse mode shape of the structure, $\phi_{r\gamma}(\Delta x)$, segment by segment as we sweep through $x = 0$ to L_n , from the root to the tip of the structure. Thus, the mode shape, $\phi_{r\gamma}(\Delta x)$, given in equation (21) is only valid within the γ^{th} beam segment and for the r^{th} mode. Upon assembling all the individual segmental modes, we get the complete mode shape function of the structure, $\phi_r(x)$, which defines the mode shape at any point within the geometric boundary of the entire structure, in the longitudinal direction.

The values of k_1, k_2 and σ can be determined for different cases.

Case 1: $U_{5,2} \neq 0$

$$k_1 = \frac{U_{5,5}}{U_{5,2}}, k_2 = \frac{U_{5,6}}{U_{5,2}}, \sigma = \frac{U_{6,2}U_{5,5} - U_{6,5}U_{5,2}}{U_{6,6}U_{5,2} - U_{6,2}U_{5,6}} \quad (23)$$

Case 2: $U_{6,2} \neq 0$

$$k_1 = \frac{U_{6,5}}{U_{6,2}}, k_2 = \frac{U_{6,6}}{U_{6,2}}, \sigma = \frac{U_{6,2}U_{5,5} - U_{6,5}U_{5,2}}{U_{6,6}U_{5,2} - U_{6,2}U_{5,6}} \quad (24)$$

Case 3: $U_{5,2} = U_{6,2} = 0$

$$k_1 = 0, k_2 = 0, \sigma = \frac{-U_{6,5}}{U_{6,6}} \quad (25)$$

It is to be noted that for a particular known modal frequency ω_r , the elements of the global transfer matrix U are all constants. As a result k_1, k_2 and σ which are derived from U are also constants and have the same value for every segment of the entire structure. It is also interesting to note that the transverse modal shape function obtained through this procedure is also piecewise defined in the sense that each of the discrete segment has its own shape function which is different from the segments adjacent to it. However, these shape functions inherently ensure continuity at the interface of every segment to provide a continuous modal shape function across the entirety of the structure.

Once the TMM has been used to retrieve the modal shape functions corresponding to each modal natural frequency, ω_r , the modal mass and stiffness matrices can be formulated for use in the system equations of motion. It has been shown [24] that the modal mass and stiffness matrix can be readily formulated from the modal shape functions, material properties, and geometry parameters as

$$M_{r,s} = \sum_{j=1}^n (\rho A)_j \int_{V_j} \phi_{rj}(\Delta x) \phi_{sj}(\Delta x) dV_j \quad (26)$$

$$K_{r,s} = \sum_{j=1}^n (EI)_j \int_{V_j} \phi_{rj}''(\Delta x) \phi_{sj}''(\Delta x) dV_j \quad (27)$$

where $M_{r,s}, K_{r,s}$ represents the element at r^{th} row and s^{th} column of the modal mass matrix, $[M]$ and modal stiffness matrix $[K]$ respectively, and V_j is the total volume of j^{th} beam segment.

2.4. Electromechanical Model of the Structure

The contribution of the bimorph piezoelectric patches towards the stiffness and mass of the substrate has already been taken into account, by introducing effective bending stiffness $(EI)_j$ and effective mass per unit length $(\rho A)_j$ of the segmental containing the piezo patches. Hence, the mode shape function generated for the entire structure during TMM already incorporates the effect of the piezoelectric patches. The parameters which still needs to be defined are primarily the electromechanical coupling matrix, Θ and the capacitance matrix, C_p

$$\Theta_r = -\sum_{j=1}^n \int_{V_{p,j}} y e_p^T \phi_r(\Delta x) \psi(y) dV_{p,j} \quad (28)$$

where e_p^T is referred to as piezocoupling coefficient, which is related to piezoelectric charge coefficient d_{pq} and piezoelectric elastic modulus at constant electric field c^E as

$$e_p^T = d_{pq} c^E \quad (29)$$

Here subscripts p, q refer to the direction of the applied field and poling respectively. The capacitance matrix is given by

$$C_{p,r} = \sum_{j=1}^n \int_{V_{p,j}} \epsilon^S \psi(y) \psi(y) dV_{p,j} \quad (30)$$

where ϵ^S is dielectric constant measured at constant strain, $\psi(y)$ is the electrical field function. It is understood that the electric field function through the thickness of the host structure is considered zero and that within the piezoceramic layer is nothing but voltage over piezoceramic thickness.

Now that all the requisite matrices are obtained, it is possible to assemble them in the electromechanically coupled equations of motions for the entire structure, which can be used to capture the dynamic response of the system. Note that the structural damping is incorporated by a proportional damping assumption as in [24]. Using just lettering for matrix parenthesis (e.g. $[M] \rightarrow M$)

$$M\ddot{\underline{\eta}}(t) + C\dot{\underline{\eta}}(t) + K\underline{\eta} - \Theta v(t) = \sum_{r=1}^m \phi_r(x)^T F_r(t) \quad (31)$$

$$\Theta^T \underline{\eta}(t) + C_p v(t) = q(t) \quad (32)$$

where $F_r(t)$ represents the modal aerodynamic force acting on the complete structure due to the incident air flow, $q(t)$ is the electrical charge, $v(t)$ is the output voltage across the ends of the piezo patch terminals. In the case of a simple resistive electrical load,

$$v_r(t) = -R\dot{q}(t) \quad (33)$$

where the resistive load is R , output voltage $v_r(t)$ and rate of charge flow is $\dot{q}(t)$

Table 1. Geometrical dimensions and mechanical properties of the structure.

Parameter	Symbol	Value	Units
Elasticity Modulus	E	193	GPa
Shear Modulus	G	77.2	GPa
Material density	ρ	7880	kg/m^3
Sheet metal thickness	t	0.38	mm
Beam length	l_b	168.12	mm
Beam width	w_b	26	mm
Flap length	l_f	36	mm
Flap span	w_f	122	mm
Flap-hinge connecting length	l_c	2.5	mm
Overall hinge length	l_h	22.88	mm

Table 2. Electromechanical properties and geometric dimensions of Mide QP 16N.

Parameter	Symbol	Value	Units
PZT modulus	c^E	67	<i>GPa</i>
PZT density	ρ_p	7800	<i>kg/m³</i>
PZT length	l_p	44	<i>mm</i>
PZT thickness	t_p	0.127	<i>mm</i>
PZT width	w_m	25.4	<i>mm</i>
Epoxy matrix thickness	t_m	0.0635	<i>mm</i>
Total PZT capacitance (bimorph)	C_p	245	<i>nF</i>
PZT strain coefficient	d_{31}	-190	<i>pm/V</i>
Constant strain permittivity	ϵ^S	15.05	<i>nF/m</i>

3. MODEL VALIDATION AND VERIFICATION

In the FE analysis the actual model is simplified such that the epoxy matrix of the piezoelectric patches is neglected for achieving consistency with the analytical model. In order to verify the applicability and accuracy of the structural modeling technique, the natural frequencies and mode shapes of the structure are determined and validated with FE and experimental results.

The material properties and geometric dimensions of the structure are provided in **Table 1** whereas the electromechanical properties of the piezo patches and its dimensions are provided in **Table 2**. Note that the length of the PZT provided in **Table 2** takes into account of the clamped portion.

Applying the parameters from the **Table 1** and **Table 2**, the short circuit natural frequencies of the system can be analytically determined after decoupling the electrical and the structural dynamics by setting $v(t) = 0$ in equation (31). It can be seen from table 3 that the first three bending natural frequencies of the system obtained analytically are very close to the natural

frequencies predicted using a short circuited model used in FE simulations of the full structure. It is found that the maximum deviation is observed in the first mode, consistent with the published work [23].

Table 3. Verification of analytically obtained short circuit natural frequencies of the system.

Mode number	FEA (Hz)	Analytical (Hz)	FEA-Analytical Deviation %
1	2.89	2.95	2.08
2	13.26	13.48	1.66
3	52.51	53.33	1.56

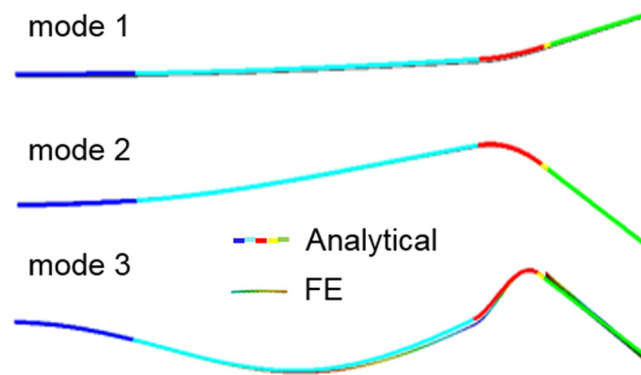


Figure 7. Comparison of Mode Shapes obtained through TMM with FE simulation. Colors in the analytical model correspond to the different segments of the structure used in TMM modeling.

The transverse beam mode shapes corresponding to the first three natural frequencies of the system has been compared with FE results in **Figure 7**. It can be seen that the analytically obtained mode shapes of the first two system natural frequencies almost completely overlaps the mode shape obtained through FE analysis. The analytically obtained mode shape corresponding to the third natural frequency is able to capture the complicated mode shape of

the entire structure with minor deviation. FE, unlike this analytical model, is not just restricted to beam mode shapes corresponding to the transverse displacement, but it also predicts the out of plane mode shapes. In the third mode it predicts the transverse bending of the flap along its span or width which is not captured by the analytical model and is the primary source of deviation.

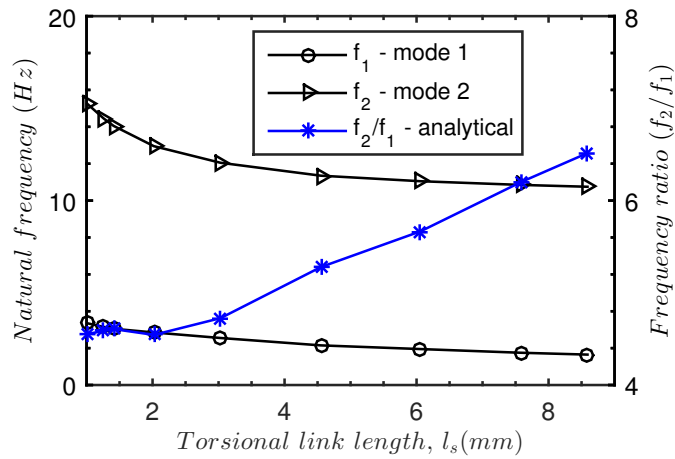


Figure 8. Effect of the geometric parameter like the torsional link length on the modal natural frequencies of the system.

As discussed previously, the effect of the flexure stiffness on the heaving and the pitching natural frequencies of the system is shown in **Figure 8**. Keeping the overall length of the structure and the flexure segment constant, only the length of the torsional link is modified to affect the torsional stiffness of the individual link and therefore modifying the overall bending stiffness of the flexure segment (equation (4)). The change in rotational stiffness of the torsional links non-linearly affects the heaving and the pitching frequencies, providing an opportunity to finely tune the structure.

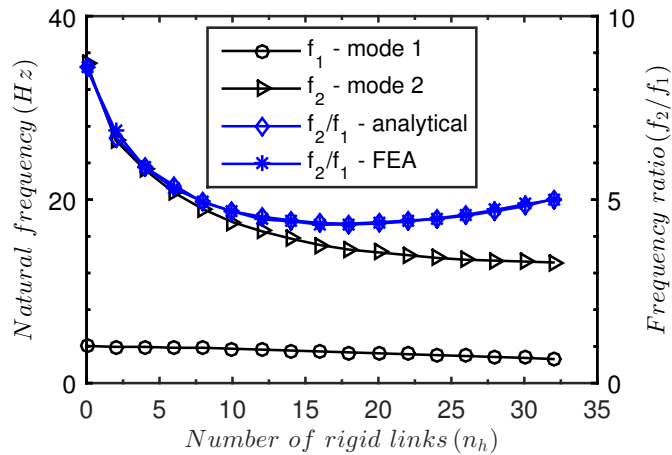


Figure 9. Effect of the geometric parameter like the number of rigid links on the modal natural frequencies of the system.

Additionally, parameter n_h which represents the number of rigid links is varied from 0 to 32 and the corresponding first two natural frequencies have been plotted in **Figure 9**. It can be observed that the frequency ratio is at a minimum at $n_h = 18$ and varies significantly from 8.63 to 5.02 with increasing rigid links. Once again the overall dimensions of the device has been kept constant and the change in length of the flexure segment is compensated by a corresponding change in the length of the beam segment. It is to be noted that at $n_h = 0$, representing the absence of the flexure, the beam segment connects directly with the flap connector segment. The frequency ratios obtained analytically are now compared with FE simulation primarily to verify the analytically obtained natural frequencies for number of links below 4 where it ceases to behave like a flexure and behaves predominantly like a beam. The analytical results show a close agreement with FE results and it can be seen that varying the number of rigid links provides a greater control over the range of frequency ratio than varying

the torsional link length. It is advantageous to be able to perform such tuning as this provides the flexibility to control the modal convergence flutter phenomenon, increasing or decreasing the cut in velocity and frequency, by either spacing the natural frequencies further apart or bring them closer to each other.

4. Experimental Setup and Results

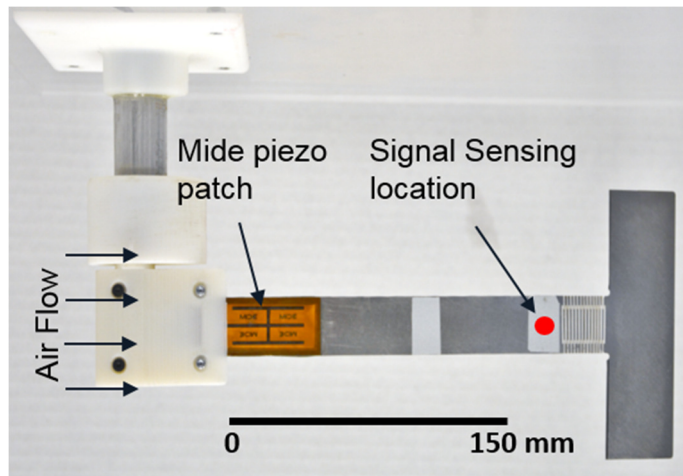


Figure 10. Physical structure as mounted in the wind tunnel test section. Beam deflection response is measured at the point specified in **Figure 1**.

The experiments discussed in this thesis were all performed in a low turbulence, open circuit wind tunnel having a maximum wind speed of 13.8 m/s and a test sectional volume of 25x25x100 cm. A Polytec OFV 503 laser vibrometer was used to measure the vibrational displacement at 9.5mm upstream from the tip of segment 2. An Agilent DSO X2004A oscilloscope was used for signal visualization and recording. The natural frequencies of the

structure were extracted from the vibration signals recorded by the oscilloscope by performing a FFT in MATLAB.

Table 4. Comparison of experimental and analytical natural frequencies.

Mode number	Open Circuit (Hz)		Short Circuit(Hz)	
	Experimental	Analytical	Experimental	Analytical
1	2.68	2.99	2.69	2.95
2	12.79	13.68	12.64	13.48

The actual physical model is set up in the wind tunnel as shown in **Figure 10** such that a pair of Mide QP16N quickpacks are laminated at the root of the structure in a bimorph configuration. Now with the setup mentioned above the natural frequencies of the system at no flow condition are obtained experimentally for both open circuit and closed circuit conditions and compared with the analytical model using equations (31)–(33).

It can be observed from **Table 4** that the measured natural frequencies show greater deviation from both the FE (**Table 3**) and analytical results, with experimental measurements consistently showing lower frequency values. It is also seen that the analytically obtained open circuit natural frequency is marginally higher than the short circuit natural frequency. This deviation can be primarily attributed to manufacturing defects and variations in the experiment. The laser-cut flexure segment shows some visible distortion (**Figure 2**) of the geometric dimensions, especially in the dimensions of the torsional links. The close agreement with the FE model shows the accuracy of the analytic method, while the deviation from the experimental measurement points to the need for dimensional accuracy in fabrication.

4.1. Modal Convergence Investigation

The aeroelastic flutter phenomenon under discussion occurs due to an aerodynamically-driven interaction between the modes of the structure. As wind speed is increased, the affected modes behave analogously to the heaving and pitching degrees of freedom of a classical aeroelastic typical section and undergo a frequency convergence phenomenon, consistent with observations reported in other aeroelastic energy harvester designs [3, 4]. Wind tunnel testing was carried out to experimentally measure the frequency behavior of the first two natural modes of the structure under varying wind speeds. It was observed that with increasing wind speed the modal frequencies corresponding to mode 1 and mode 2 approach each other and converge at a well-defined wind speed. This speed is known as the cut-in wind speed and it represents the onset of flutter in the system. The frequencies of the system were recorded after externally exciting the system by providing a 50 V DC pulse through the terminals of the piezoelectric patch laminated at the root of the structure. However, once flutter sets in and the system exhibits LCOs there was no further need to externally excite the system.

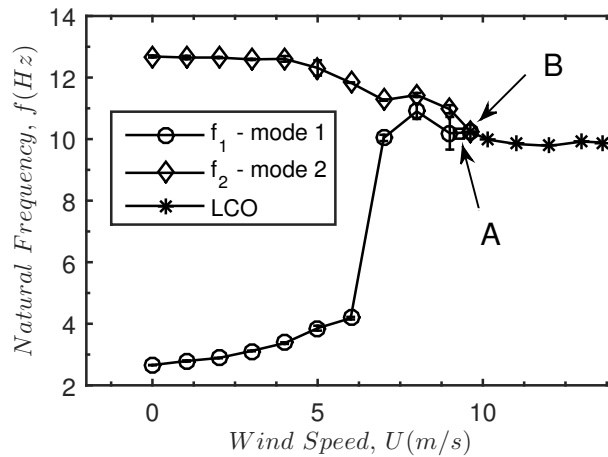


Figure 11. Effect of varying wind speeds on first two natural frequencies of the structure, showing (A) externally excited and (B) self-excited flutter locations. This plot also shows the estimated error in measurements via error bars representing one SD in each direction vertically.

The modal convergence plot, as expected, shows that the cut-in flutter wind speed for an externally excited system is marginally lower than the self-excited flutter at 9.30 and 9.65 ms^{-1} of incident wind speeds respectively. This can be clearly observed in **Figure 11**. This behavior indicates that the LCOs in this system emerge due to a Hopf bifurcation of the subcritical type [25]. In this type of bifurcation, there is a coexistence of stable equilibrium and an oscillating limit cycle at low wind speeds, introducing a sensitivity to initial conditions or external disturbances. One interesting observation in the modal convergence plot is that beyond the cut-in wind speed the system flutter frequency remains nearly constant with increasing incident wind speed. Even when the wind speed is increased from 9.65 m s^{-1} at flutter point (B) to 13.6 m s^{-1} the frequency deviates within a tight limit of 4% of its cut-in frequency. This

observation is unlike the previous work shown by Bryant et al [4] for systems with traditional hinge joints which showed a stronger increase in flutter frequency with wind speed.

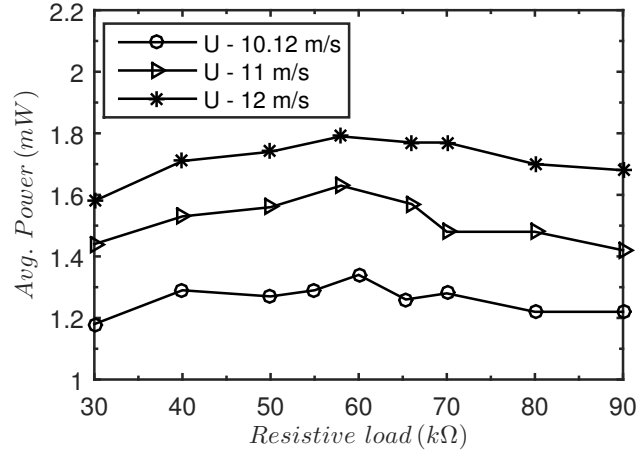


Figure 12. This figure plots the average power output of the structure as a function of resistive load for three different wind speeds, U .

4.2. LCO Investigation

It has been shown by Guyomar et al. [19] that for weakly electromechanically coupled systems, the optimized resistive load is given by

$$R_{opt} = \frac{1}{C_p \omega} \quad (34)$$

where ω represents the angular frequency of vibration of the system.

A load resistance sweep is performed, across three different wind speeds and the corresponding average power output of the system is plotted in **Figure 12**. The optimized resistances calculated for these wind speeds vary within a small range of 64–65 $k\Omega$. It is observed from **Figure 12** that all the three wind speeds shows an increased power output at

resistive loads around $60\text{ k}\Omega$ which is close to the calculated value. It is also seen that even though the resistive loads are varied over a wide range the average power output of the system does not vary appreciably.

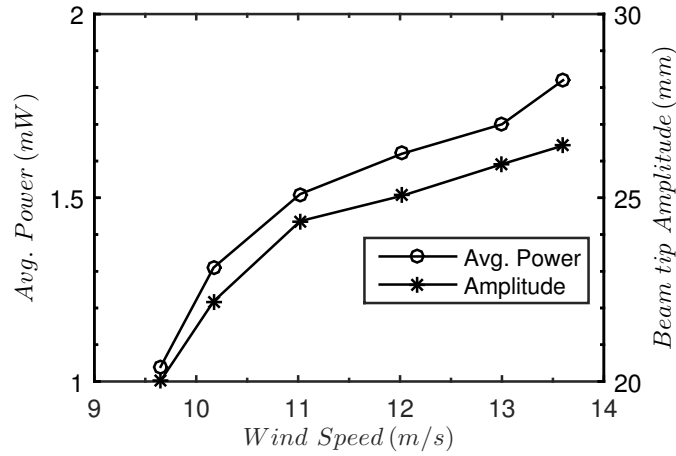


Figure 13. This figure plots the beam tip response and average power output of the structure as a function of wind speed. The beam tip deflection is measured at the point specified in **Figure 10**.

Hence, for every wind velocity beyond the flutter point, the resistive load was optimized according to equation (34) and the variation of average power output was plotted against wind-speed as shown in **Figure 13**. It is observed that the average power output increases with increasing wind speed even though the system frequency remains virtually constant beyond cut-in wind speed. The system generates a power of 1.82 mW at around 13.6 m s^{-1} of wind speed, which is the maximum within the test envelope, beyond which further experimentation was not possible owing to the speed limitations of the wind tunnel. The non-optimized system generates $1.04\text{--}1.82\text{ mW}$ of power which in itself can be used to power low powered electronic

devices. The power output of this device is of the same order as that observed by Bryant et al (2011) with his aeroelastic flutter energy harvester with a traditional hinge.

The flutter point or cut in wind speed theoretically represents a point where the aerodynamic, structural and electrical damping of the system are overcome by destabilizing aerodynamic forces which allows flutter to set in. This destabilization of the system results in growing amplitude of flutter vibration which is only limited by the presence of structural and aerodynamic nonlinearities which enables the system to flutter with a constant frequency and amplitude over time, for a given range of flow conditions. In order to understand the limit cycle behavior of the system, the amplitude response of the tip of the beam segment has been experimentally characterized. Consistent with published research [4], the system amplitude is observed to be bounded and constant for any particular wind speed beyond the flutter point. When the beam deflection is plotted against increasing incident wind speed as shown in **Figure 13**, it is observed to follow the trend of average power output.

5. Conclusion

This article presents and investigates the concept of a flow energy harvester with a compliant flexure joint. Analytical methods are developed for modeling a complicated, yet readily fabricated, flexure geometry and for incorporating it into an overall structural model. The methods proposed here will allow designers to create flow energy harvesters that share the one-piece construction, low friction, and robustness of simple flag-like structures, but also take advantage of the ability to perform aeroelastic tailoring by tuning frequencies and mode shapes as in a hinged structure. The approach utilizes the transfer matrix methodology, a versatile and computationally fast formulation that can incorporate an arbitrary number of geometric and

material discontinuities. The structural model of both the flexure and the complete structure are validated against FE simulations.

Wind tunnel testing of a proof-of-concept device demonstrates that it is possible to create an aeroelastic energy harvester based on a compliant flexure design and further validates the structural model results. The experiments show a well-defined critical cut-in wind speed, below which the structure ceases to exhibit flutter and above which stable LCOs are observed. Empirical measurements of the structural response below the critical wind speed confirm that the aerodynamic forces lead to speed-dependent natural frequencies for the first two modes of the structure, and that the observed LCO are the result of a modal-convergence flutter instability. The LCO power output of the system under an optimized resistive load increases from 1.04 mW just above cut-in to 1.82 mW at the maximum speed of the wind tunnel. This shows that the current, un-optimized system can be used to supply low power electronic devices. It is also interesting to note that the sensitivity of LCO frequency to incident wind speed observed in this device is lower than in previous flutterbased flow energy harvesters. In fact, the frequency of oscillations remain almost constant during LCO, even when flow speed is varied by more than 40%. This may be advantageous in applying more advanced power electronics that rely on phase synchronization. In addition, because flexures are readily fabricated using micro-fabrication techniques like chemical etching, the design presented here is readily miniaturized to small scales and lower Reynolds number flow regimes.

REFERENCES

- [1] Shashank P and Inman D J 2009 *Energy Harvesting Technologies* ed S Priya and D J Inman (Boston, MA: Springer US)
- [2] Li S and Lipson H 2009 Vertical-Stalk Flapping-Leaf Generator for Wind Energy Harvesting *Volume 2: Multifunctional Materials; Enabling Technologies and Integrated System Design; Structural Health Monitoring/NDE; Bio-Inspired Smart Materials and Structures* (Ithaca: ASME) pp 611–9
- [3] De Marqui C and Erturk A 2012 Electroaeroelastic analysis of airfoilbased wind energy harvesting using piezoelectric transduction and electromagnetic induction *J. Intell. Mater. Syst. Struct.* **24** 846–54
- [4] Bryant M and Garcia E 2011 Modeling and Testing of a Novel Aeroelastic Flutter Energy Harvester *J. Vib. Acoust.* **133** 011010
- [5] Bibo A and Daqaq M F 2013 Energy harvesting under combined aerodynamic and base excitations *J. Sound Vib.* **332** 5086–102
- [6] Dunnmon J A, Stanton S C, Mann B P and Dowell E H 2011 Power extraction from aeroelastic limit cycle oscillations *J. Fluids Struct.* **27** 1182–98
- [7] Tang L, Païdoussis M P and Jiang J 2009 Cantilevered flexible plates in axial flow: Energy transfer and the concept of flutter-mill *J. Sound Vib.* **326** 263–76
- [8] Giacomello A and Porfiri M 2011 Underwater energy harvesting from a heavy flag hosting ionic polymer metal composites *J. Appl. Phys.* **109** 084903
- [9] Kwon S D 2010 A T-shaped piezoelectric cantilever for fluid energy harvesting *Appl. Phys. Lett.* **97** 57–60
- [10] Bryant M, Wolff E and Garcia E 2011 Aeroelastic flutter energy harvester design: the sensitivity of the driving instability to system parameters *Smart Mater. Struct.* **20** 125017
- [11] Bryant M, Schlichting A D and Garcia E 2013 Toward efficient aeroelastic energy harvesting: device performance comparisons and improvements through synchronized switching *Proc. SPIE 8688, Active and Passive Smart Structures and Integrated Systems* vol 8688, ed H Sodano p 868807
- [12] Polit S and Dong J 2009 Design of high-bandwidth high-precision flexure-based nanopositioning modules *J. Manuf. Syst.* **28** 71–7

- [13] Xu W and King T 1996 Flexure hinges for piezoactuator displacement amplifiers: flexibility, accuracy, and stress considerations *Precis. Eng.* **19** 4–10
- [14] Lobontiu N, Garcia E and Canfield S 2004 Torsional stiffness of several variable rectangular cross-section flexure hinges for macro-scale and MEMS applications *Smart Mater. Struct.* **13** 12–9
- [15] Dirksen F, Anselmann M, Zohdi T and Lammering R 2013 Incorporation of flexural hinge fatigue-life cycle criteria into the topological design of compliant small-scale devices *Precis. Eng.* **37** 531–41
- [16] Hodges D H and Pierce G A 2011 *Introduction to Structural Dynamics and Aeroelasticity* ed W Shyy and V Yang
- [17] McCarthy J M, Deivasigamani A, John S J, Watkins S, Coman F and Petersen P 2013 Downstream flow structures of a fluttering piezoelectric energy harvester *Exp. Therm. Fluid Sci.* **51** 279–90
- [18] ElDarwish I A . and Johnston B G 1965 Torsion of structural shapes *J. Struct. Div. ASCE* **19** 203–28
- [19] Pestel E C and Leckie F A 1963 *Matrix Methods in Elasto-Mechanics* (New York: McGraw Hill Book Company Inc.)
- [20] Shen J Y, Abu□Saba E G, McGinley W M, Sharpe L and Taylor L W 1994 Continuous Dynamic Model for Tapered Beam-Like Structures *J. Aerosp. Eng.* **7** 435–45
- [21] Karami M A and Inman D J 2012 Parametric study of zigzag microstructure for vibrational energy harvesting *J. Microelectromechanical Syst.* **21** 145–60
- [22] Attar M 2012 A transfer matrix method for free vibration analysis and crack identification of stepped beams with multiple edge cracks and different boundary conditions *Int. J. Mech. Sci.* **57** 19–33
- [23] Wickenheiser A M 2012 Eigensolution of piezoelectric energy harvesters with geometric discontinuities: Analytical modeling and validation *J. Intell. Mater. Syst. Struct.* **24** 729–44
- [24] Sodano H A, Park G and Inman D J 2004 Estimation of electric charge output for piezoelectric energy harvesting *Strain* **40** 49–58

- [25] Strogatz S H 2001 *Nonlinear Dynamics And Chaos: With Applications To Physics, Biology, Chemistry, And Engineering (Studies in Nonlinearity)* (Cambridge: Westview Press)

This thesis is based on:

Chatterjee P and Bryant M 2015 Structural modelling of a compliant flexure flow energy harvester *Smart Mater. Struct.* **24** 094007